JMEPEG
https://doi.org/10.1007/s11665-021-06123-2

©ASM International
1059-9495/$19.00

Enhanced Wear Resistance of AISI-316 Steel by Low-Temperature Molybdenum Cathodic Cage Plasma Deposition

M. Naeem, V.C. Fortaleza, P.L.C. Serra, C.L. Lima, T.H.C. Costa, R.R.M. Sousa, J.C. Díaz-Guillén, and Javed Iqbal

Submitted: 7 April 2021 / Revised: 19 June 2021 / Accepted: 14 July 2021

The austenitic stainless steels are extensively used in industrial applications owing to their outstanding corrosion resistance. However, their use is limited in several applications due to their poor tribological properties and the need to be upgraded. This study investigates the tribological behavior of molybdenum oxide coating on AISI-316 steel deposited by low-temperature cathodic cage plasma deposition (CCPD). The wear behavior is investigated by a ball-on-disc wear tester which reveals the outstanding friction reducing capability and wear resistance of molybdenum oxide film. The film deposited by keeping on floating potential only contains the MoO_3 phase, while mixed phases of MoO_3 and Fe_2O_3 are found on the film deposited by cathodic potential. This is also supported by Raman analysis. Moreover, the successful deposition of MoO_3 on floating potential reveals this system efficiency to deposit this coating on insulators. This study shows that MoO_3 coating by CCPD can enhance tribological features and act as a solid lubricant coating. The CCPD system exhibits high deposition efficiency; no complicated equipment is required in this system; the deposited film is quite homogeneous, the low processing temperature is required, the rough vacuum is required, and this system compatibility with industry makes this study more effective to fulfill industrial needs.

Keywords cathodic cage plasma deposition, iron oxide, molybdenum oxide, wear resistance

1. Introduction

Transition metal oxides, including molybdenum oxides, are widely used in numerous applications, such as photochromicity, chemical sensing, as a catalyst in oxidation-reduction reactions, and electrochromicity (Ref 1). Also, such coated materials are used in lithium batteries, display devices, smart windows, anti-dazzling film, and sensors (Ref2). Due to the broad range of applications, various techniques are adopted to synthesize these films, including wet-chemistry (Ref 3), RF/DC magnetron sputtering (Ref 4), solgel (Ref 5), evaporation (Ref 6), ion-beam assisted deposition (Ref 7, pulsed laser deposition (Ref 8, and plasma focus device (Ref 9). However, it is a serious concern to adopt those techniques that require simple equipment with the least processing cost and are eco-friendly. The conventional deposition techniques require complicated equipment, employ hazardous chemicals (Ref 10), present low-deposition efficiency (Ref 11), have high processing costs (Ref 11), and are not favorable for industrial-scale applications (Ref 12). The above shortcomings demand novel techniques to deposit molybdenum oxide films for large-scale utilization.

The deposition of oxide films on various metallic materials, including steel, is widely reported by conventional plasma processing techniques (Ref 13, 14). In the conventional plasma processing technique, samples are placed on the cathodic potential, directly bombarded by the energetic ions of oxygen plasma. As a result, sputtered target material combines with oxygen atoms and adsorb on the target material (Ref 13). This intensive direct ions bombardment causes several issues, including samples overheating, border effect, hollow cathode effect, damaging the sample's surface, and deposited film is not homogeneous (Ref 15). Furthermore, assisted with conventional plasma processing technique, only the oxide films of substrate material (due to direct ions bombardment on the substrate) can be deposited. The oxide film of some other material cannot be deposited. In this regard, around two decades ago, a novel cathodic cage plasma/ active screen plasma technique was introduced, which contains a metallic screen at cathodic potential (which is called cathodic cage) surrounding the substrate (which is at floating potential) (Ref 16). As no direct bombardment of ions is involved, overheating or border effect can be eliminated or reduced.

The cathodic cage plasma technique involves cage material sputtering, reaction with processing gasses, and re-deposition on the substrate (Ref 17). Thus, the oxide films of cathodic cage material can be synthesized on the substrate; due to this feature, this technique is also termed as cathodic cage plasma deposi-

---

M. Naeem, Department of Physics, Women University of Azad Jammu and Kashmir, Bagh, Pakistan; **V.C. Fortaleza**, Mechanical Departament, Federal University of Piaui (UFPI), Teresina, PI, Brazil; **P.L.C. Serra, C.L. Lima,** and **R.R.M. Sousa**, Advanced Materials Interdisciplinary Laboratory (LIMAV) - Postgraduate Program in Materials Science and Engineering, Federal University of Piaui (UFPI), Teresina, PI, Brazil; **T.H.C. Costa**, Mechanical Department, Federal University of Rio Grande do Norte (UFRN), Natal, RN, Brazil; **J.C. Díaz-Guillén**, CONACYT-Corporación Mexicana de Investigación en Materiales, 25290 Saltillo Coahuila, México; and **Javed Iqbal**, Department of Physics, University of Azad Jammu and Kashmir, Muzaffarabad, Pakistan; and University of Latvia, Raina bulvaris 19, Riga LV-1586, Latvia. Contact e-mails: mnaeem@wuajk.edu.pk and naeem.plasma@gmail.com.

tion (CCPD) technique. The CCPD technique is widely used to synthesize numerous materials, including chromium (Ref 18), nickel (Ref 19), niobium (Ref 20), silver (Ref 21), copper (Ref 22), and titanium (Ref 23). Previously we reported the deposition of aluminum nitride on steel samples using the aluminum cathodic cage, and homogenous film with excellent tribological and corrosion properties was obtained (Ref 24, 25). Later on, a molybdenum cathodic cage was used to deposit molybdenum oxide and nitride films on steel samples, and a homogeneous film was obtained [2]. As stated in the literature (Ref 26), molybdenum oxide film acts as a solid lubricant, and thus it is essential to evaluate the wear properties of molybdenum oxide films deposited by CCPD. Furthermore, the molybdenum oxide films are used in photocatalysis and optical technologies (Ref 27), and thus this coating is also essential for insulator materials. To investigate the suitability of CCPD to deposit molybdenum oxide on insulators, the effect of samples biasing (floating and cathodic potential) is also necessary to be examined. It is commonly reported that high-temperature processing of austenite-matrix steel samples causes the chromium nitrides precipitation, which deteriorates the corrosion resistance of film (Ref 28. Thus, low-temperature CCPD is preferable to retain the corrosion resistance of austenitic stainless steel and to improve the tribological properties.

Here, low-temperature (673 K) CCPD equipped with molybdenum cage is used to deposit molybdenum oxide on AISI-316 steel by keeping samples on floating and cathodic potential. The deposited coatings are examined by X-ray diffraction, Raman spectroscopy, scanning electron microscopy, wear analysis by a ball-on-disc tester, and adhesion by Rockwell-C indentation test.

2. Experimental Details

Samples of austenitic stainless steel (AISI-316) having a thickness of 5 mm and surface area of 20 × 20 mm^2 acquired from Villares Metals were used. The elemental composition of samples in the annealed state was (weight %): 17% Cr, 12% Ni, 2.2% Mo, 0.03% C, and iron (balance). Prior to processing, samples were mirror-polished by a mechanical polishing machine equipped with silicon carbide papers and diamond paste.

The processing chamber used in this study is shown in Fig. 1. Some of the samples were directly kept on the cathodic base plate (cathodic potential) and others on the insulator plate to kept them on floating potential. We used a molybdenum cathodic cage with a diameter of 70 mm, a height of 40 mm, and equally distributed holes of 8 mm diameter. Prior to film deposition, the samples were sputter-cleaned for 1 h using the hydrogen/argon gas mixture at a temperature of 623 K and pressure of 80 Pa. The oxidation of samples was done assisted with the oxygen/hydrogen mixture (equal concentration) at a low temperature of 673 K for 5 h and a pressure of 70 Pa.

The samples were analyzed by X-ray diffraction equipped with a CuKα-radiation source, operated by the current of 40 mA and voltage of 45 kV. The surface morphology and cross-sectional examination was done by SEM analysis (Tescan Mira 3 model) and surface elemental composition by elemental dispersive spectroscopy (Bruker, model Xflash). The adhesion of film was evaluated by Rockwell C technique according to VDI 3198 standard using Isize durometer (model ISH-BRV).

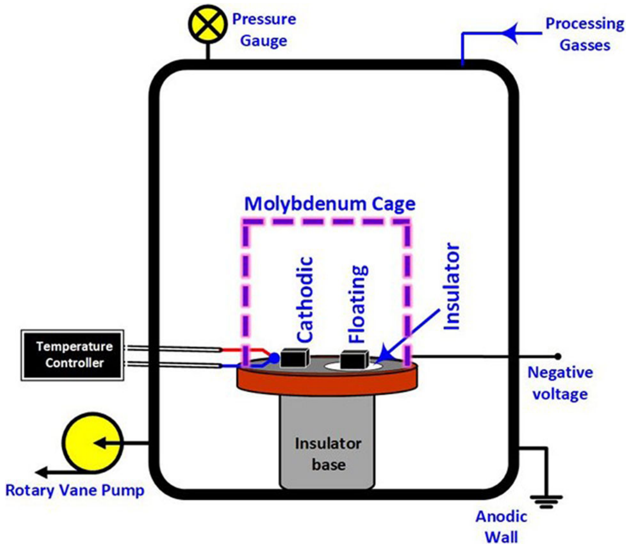

Fig. 1 Schematic diagram of CCPD reactor for synthesis of molybdenum oxide film at floating and cathodic potential

The Raman analysis was conducted assisted with a micro-Raman Senterra Bruker spectrometer. It was equipped with a charge-coupled device (CCD) system and had a resolution of Raman of 3 cm^{-1}. The system consists of a 785 nm laser and a power of 25 mW. The wear performance of deposited films was analyzed by ball-on-disc wear tester consisted of an alumina ball of 6 mm diameter. In this analysis, the normal load of 2 N, speed of 10 cm/s, sliding distance of 200 m and radius of wear track 2 mm were used.

3. Results and Discussion

3.1 XRD Analysis

The phase structures of base material and samples processed at floating and cathodic potential is shown in Figure 2. The base sample mainly contains austenite phase (γ) with a minor amount of martensite phase (α). The martensite phase is presented in base metal as a result of transformation from austenite due to severe plastic deformation during the rolling process (Ref 29, 30). The samples of austenitic stainless steel AISI-316 used in this work are of 5 mm thickness, which was obtained by a rolling process involving a considerable strain level. Therefore, the microstructure of base material consists of austenite phase plus a quantity of martensite, which was transformed during the rolling process. Slip bands can also be appreciated to indicate dislocation gliding product of high strain (Ref 31). The microstructure of the base material is shown in Fig. 3, which indicates the presence of slip bands. These transformation phenomena from austenite to martensite, leading to a dual-phase microstructure in 316L stainless steel, have been reported as an alternative to improve the work-hardening ability and strength of these alloys (Ref 29, 30, 32). It has been reported that martensite transformation percentages from 13% to 30% for deformation between 30% and 50% when rolling is carried out at room temperature (Ref 33). On this basis and XRD peaks identification, we consider that peak at approximately 44.35° corresponds to the martensite phase,

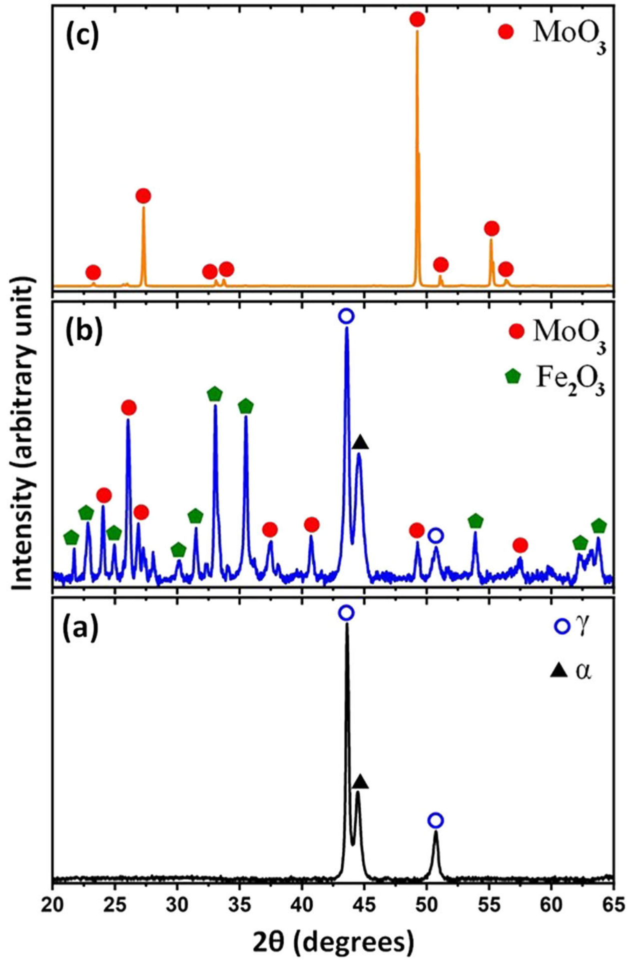

Fig. 2 XRD spectra of (a) base (untreated material), sample treated with molybdenum cage at (b) cathodic and (c) floating potentials

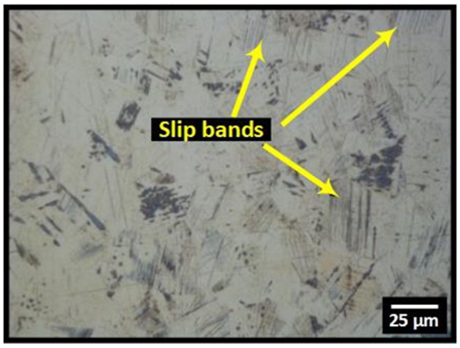

Fig. 3 Optical micrograph of base material prior to molybdenum oxide deposition

which could be slightly increased due to the polishing process carried out prior to processing (Ref 34).

In contrast, the sample treated by molybdenum cathodic cage by keeping sample on cathodic potential (Fig. 2b) contains a mixture of molybdenum trioxide and iron oxide phases following Crystallography Open Database (COD): 96-900-9670 and 96-152-8613, respectively. The co-existence of molybdenum and iron-containing peaks indicates that besides the deposition of molybdenum sputtered from the cathodic cage, another mechanism contributes. Although, in the literature, several contradictory mechanisms are presented, including Saeed et al. Ref 35), Gallo et al. Ref 36, and Hubbard et al. Ref 37 to explain the CCPD processes. The latest model is presented by Fraczek et al. Ref 17, which states that the following processes are involved in CCPD: cathodic sputtering of atoms from the cage and its admixing in plasma area, its reaction with active gasses atoms, and subsequent re-deposition on the sample surface. It clarifies the deposition of molybdenum oxide on the sample surface. The additional presence of iron oxide can be ascribed to the cathodic biasing of samples, which causes direct ions hitting on the samples. Thus its sputtering and re-deposition are also involved, like the conventional plasma processing system (Ref 38). On the other hand, the sample treated at floating potential illustrates the presence of only molybdenum oxide following COD 96-900-9670, which can be attributed to only sputtering of the molybdenum cathodic cage, as described Ref 17, 36. These findings suggest that a combination of iron oxide and molybdenum oxide can be deposited on austenitic stainless steel samples using low-temperature CCPD at cathodic potential and individual molybdenum oxide at floating potential.

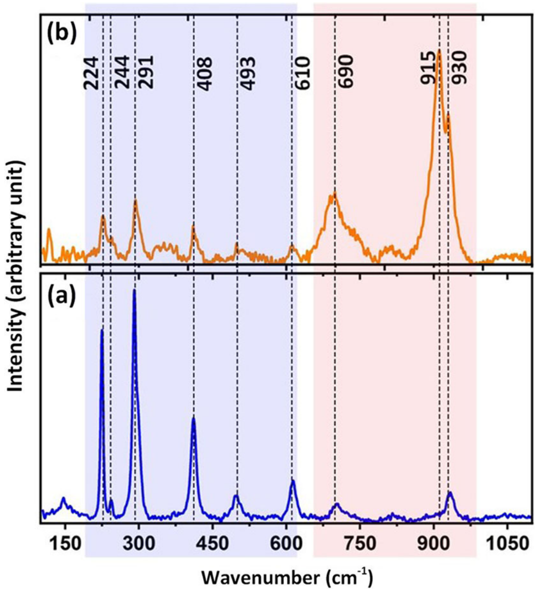

Fig. 4 Raman spectrum of treated sample with molybdenum cathodic cage by keeping at (a) cathodic and (b) floating potentials

3.2 Raman Analysis

The Raman spectra in the range of 100-1100 cm^{-1} are depicted in Fig. 4. The sample treated at cathodic potential shows that spectra mainly contain bands in the range of 200-610 cm^{-1}, corresponding to the hematite structure (Ref 39). The presence of hematite structure is an indication of sputtering from samples surface due to their cathodic potential, and its reaction with oxygen and re-deposition on samples. Besides this, it depicts the presence of less intense bands at 690 cm^{-1}, which corresponds to the scissoring vibrations of the $O-Mo-O$ bonds (Ref 40, 41). Also, less intense bands are appearing at 910 cm^{-1} and closer to it, and it is reported that bands in this range are due to $M=O$ bonds (Ref 41). Conversely, the sample treated at floating potential indicates that it mainly consists of bands at 690 cm^{-1} (corresponding to $O-Mo-O$ bonds) and an intensive band closer to 910 cm^{-1}

(corresponding to $M = O$ bonds). It shows that the sample treated at floating potential mainly consists of molybdenum and oxygen and supports molybdenum oxide formation. The dominant presence of molybdenum and oxygen can be credited to sputtering only from the molybdenum cathodic cage, and molybdenum is admixed in plasma environment, it reacts with oxygen atoms and deposited as molybdenum oxide (Ref 17). Thus, Raman analysis supports the results from XRD analysis as described above.

3.3 EDS Analysis

The results obtained from XRD and Raman analysis can be clarified by analyzing the film's elemental composition using EDS analysis. The EDS spectrum of base material and molybdenum oxide deposited sample at floating, and cathodic potential is depicted in Fig. 5. For improved reliability, EDS analysis is repeated six times, and the average spectrum is presented here. The base material shows the composition of AISI-316 steel containing iron along with alloying elements chromium, nickel, and silicon. The molybdenum oxide deposited sample at cathodic potential shows molybdenum, oxygen, and substrate material elements (iron and chromium). The coexistence of molybdenum and substrate elements is obviously due to substrate and cathodic cage sputtering. In contrast, the molybdenum oxide deposited sample at floating potential only contains molybdenum and oxygen elements deposited due to cage sputtering and its reaction with oxygen and re-deposition on the sample surface. This supports the results discussed in XRD and Raman analysis.

3.4 Adhesion Strength

The adhesion strength was analyzed by the Daimler-Benz Rockwell-C adhesion test. The adhesion strength can be characterized in six categories ranging from HF1 (excellent adhesion) to HF6 (weak adhesion). In the HF1, only small radial cracks around the indentation can be observed, and HF6 is associated with the layers delamination in the vicinity of the indentation; the intermediate classifications HF2, HF3, and HF4 are considered satisfactory, while HF5 indicate weak coating adhesion (Ref 42). The test is widely used in the thin films adhesion evaluation (Ref 43, 44); however, previous works (Ref 45, 46) have shown the satisfactory application of the technique for characterizing boride layers whose thickness is greater (up to 53 μm) than the layers deposited in this work (28–38 μm). In addition to characterizing adhesion, the test allows assessing the coating fragility by analyzing the radial cracks, which can indicate a coating fragile behavior even under satisfactory adhesion conditions (Ref 42, 45). The micrographs shown in Fig. 6 reveal that both films can be associated with the HF1 category and indicate excellent adhesion of the coating to the AISI-316 steel substrate, and also we can observe the absence of radial cracks, revealing a ductile behavior of the applied coatings and, consequently, a good cohesive force. Figure 6(a) clearly shows the material accumulation at the indentation edges in the sample treated in cathodic potential. It may reveal more remarkable plasticity of this coating compared to the deposited in floating potential.

3.5 SEM Analysis

The surface morphology of molybdenum oxide deposited at floating, and cathodic potential is depicted in Fig. 7. The base material's morphology (not shown here) contains scratches on the surface induced by samples' mechanical polishing. A substantial alteration in surface morphology is observed by varying the sample's biasing potential. The SEM image of the cathodic potential treated sample (Fig. 7a) shows that the layer is uniformly deposited on the entire surface. The high-resolution image (Fig. 7b) shows that deposited film comprises mainly agglomerated spherical particles. These particles are due

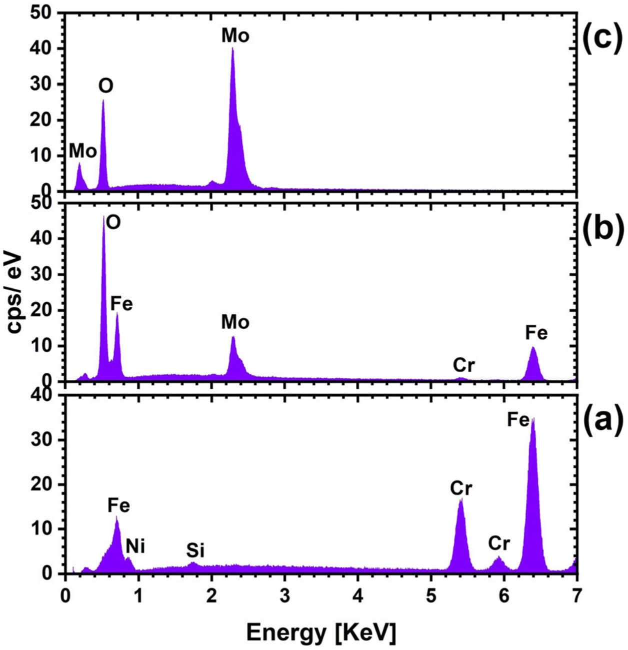

Fig. 5 EDS spectrum of (a) base, sample treated with molybdenum cage by keeping at (b) cathodic and (c) floating potentials

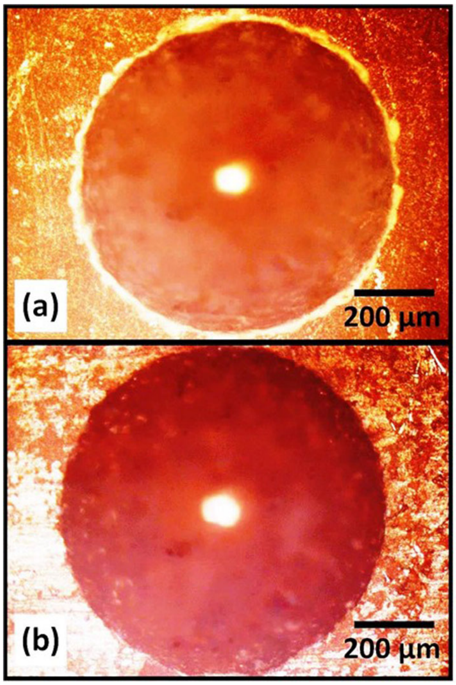

Fig. 6 Surface morphology of indents by Rockwell test of samples treated with molybdenum cathodic cage by keeping at (a) cathodic and (b) floating potentials

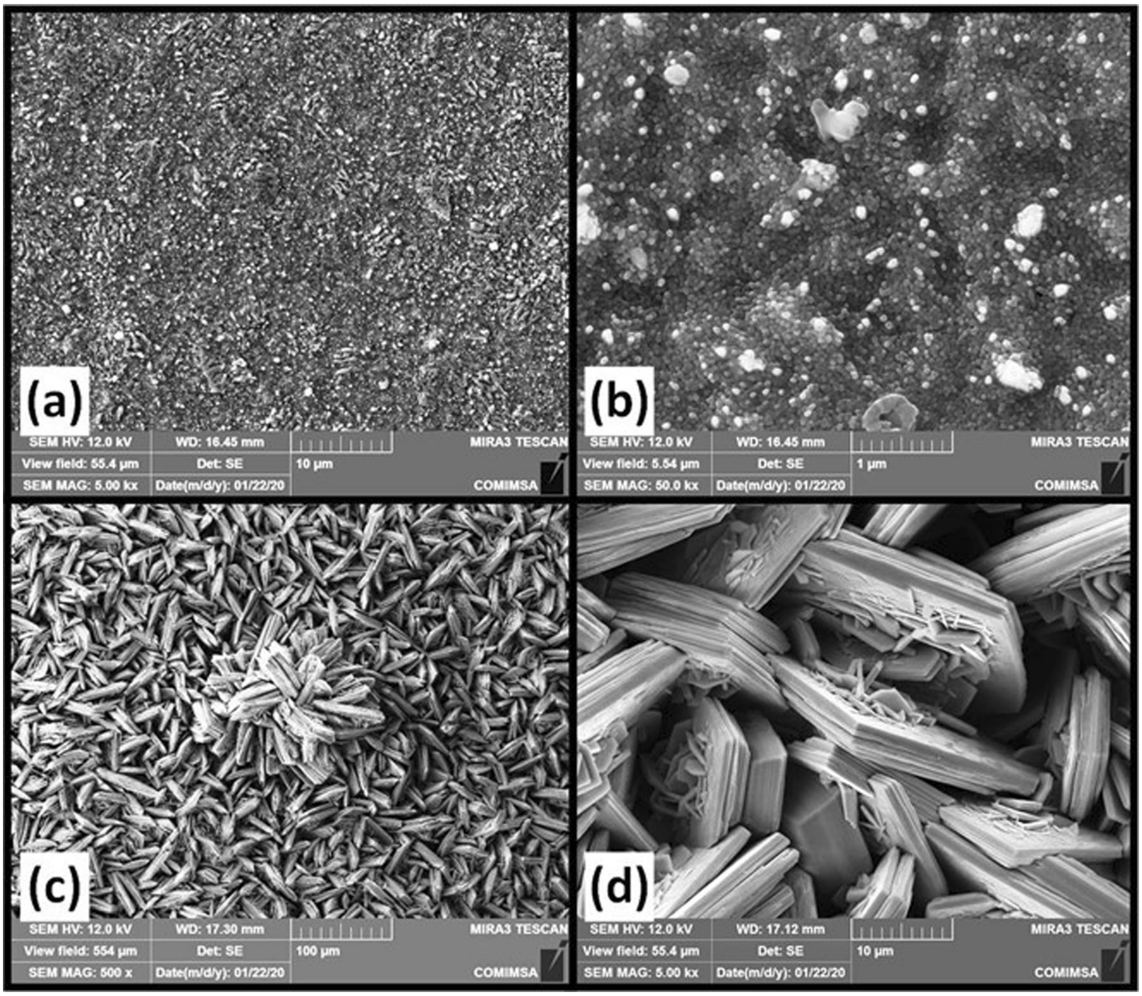

Fig. 7 Surface SEM images of samples treated with molybdenum cathodic cage by keeping at (a, b) cathodic and (c, d) floating potentials

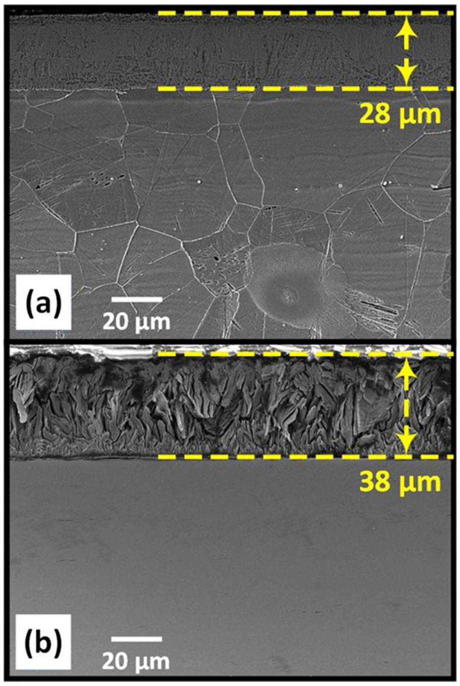

Fig. 8 Cross sections of treated samples at (a) cathodic and (b) floating potentials

to sputtering from the cage as well as from the sample surface. Such morphology for molybdenum oxide film is well-known in the literature (Ref 47). In contrast, the molybdenum oxide film deposited at floating potential (Fig. 7c, d) reveals that the whole surface is uniformly covered with micro-platelets. Such morphology for molybdenum oxide deposited samples is also following the literature [48]. The synthesized micro-platelets are primarily rectangular and are arranged parallel to each other in small regions, whereas random orientation on the sample. In fact, the morphology of film is dependent on deposition equipment and control parameters. It can exhibit numerous shapes, including elongated columns, rectangular piped, oval, needle and plates, as found in the literature (Ref 47, 49, 50).

The thickness and uniformity of deposited films are analyzed by cross-sectional SEM analysis and are presented in Fig. 8. The thickness of molybdenum oxide deposited film at cathodic potential is 28 µm and is 38 µm for floating potential. The least thickness of sample treated at cathodic potential can be ascribed to direct ions bombardment on samples surface, which causes sputtering of deposited film (Ref 51, 52). The layer deposited by placing samples on cathodic potential is quite dense due to sputtering re-deposition on the sample surface. The thickness of film deposited at floating potential is greater than cathodic potential because in this case no direct ions bombardment on surface of samples is involved. In this

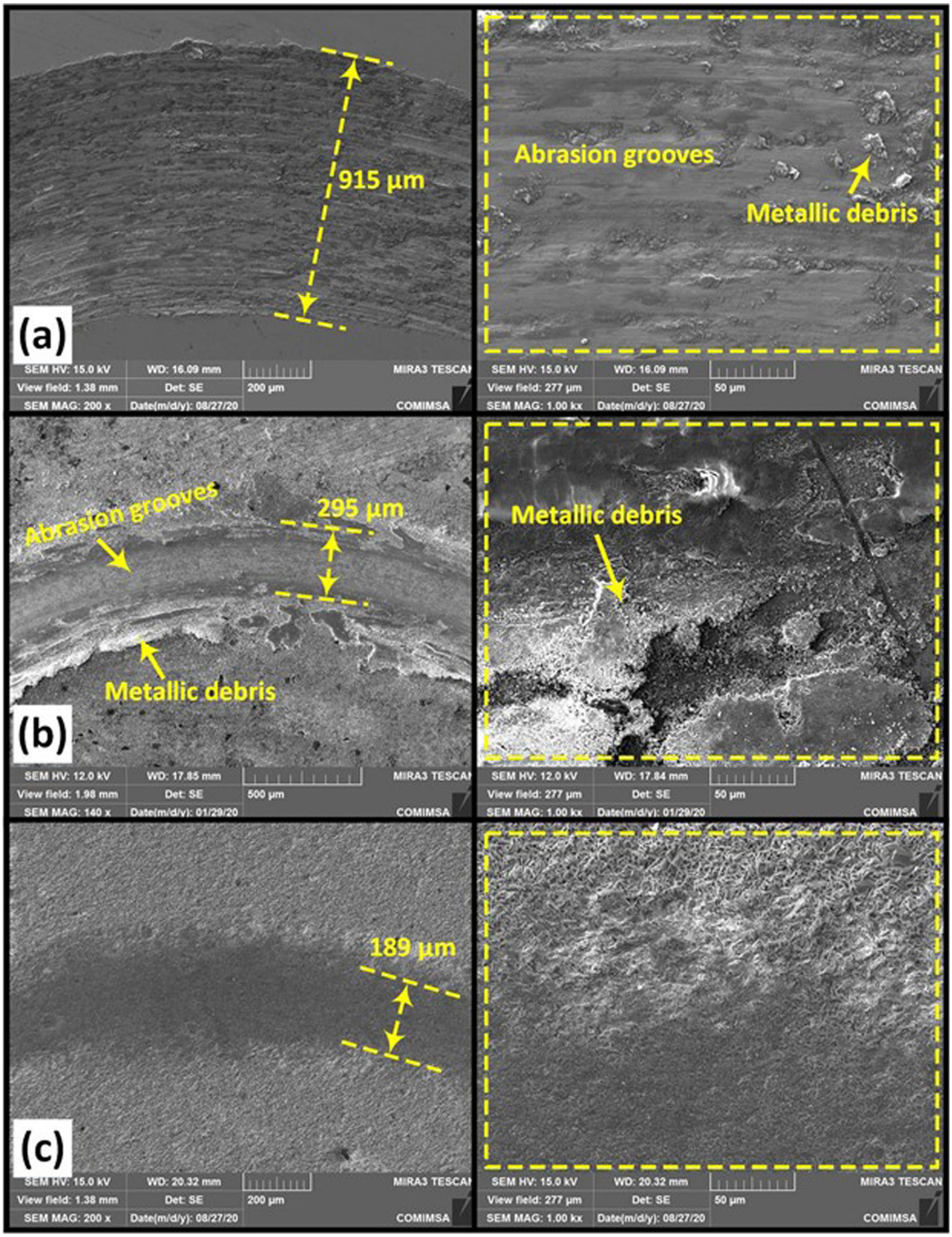

Fig. 9 Wear track images of (a) base, sample treated with molybdenum cage at (b) cathodic and (c) floating potentials

case, the sputtering only occurs from cathodic cage, and sputtered molybdenum reacts with oxygen atoms in plasma environment and molybdenum oxide is deposited on sample surface with adequate thickness. The film deposited by placing samples on floating potential is in agreement with surface SEM images. It shows that the layer is composed of micro-platelets arranged in various orientations.

3.6 Wear Test

The wear behavior of deposited films is compared using a ball-on-disc wear tester, and SEM images of wear tracks are presented in Fig. 9. The wear track of base material (Fig. 9a) reveals that the track is wide compared to other processed samples. The high-resolution images indicate the abrasion grooves are formed due to the removal of surface material, and

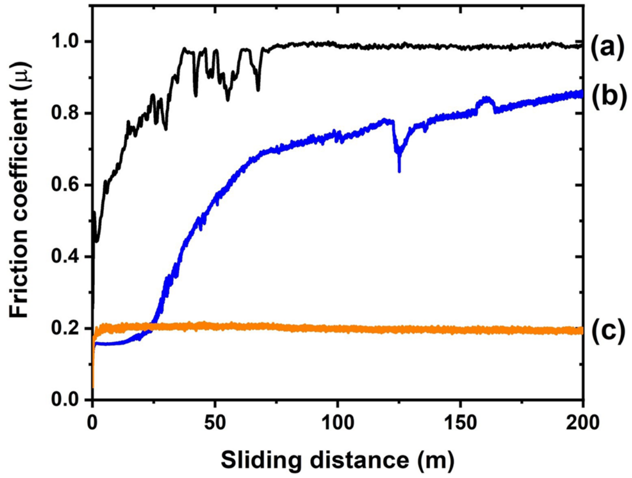

Fig. 10 Friction coefficient as a function of sliding distance of (a) base, sample treated with molybdenum cage at (b) cathodic and (c) floating potentials

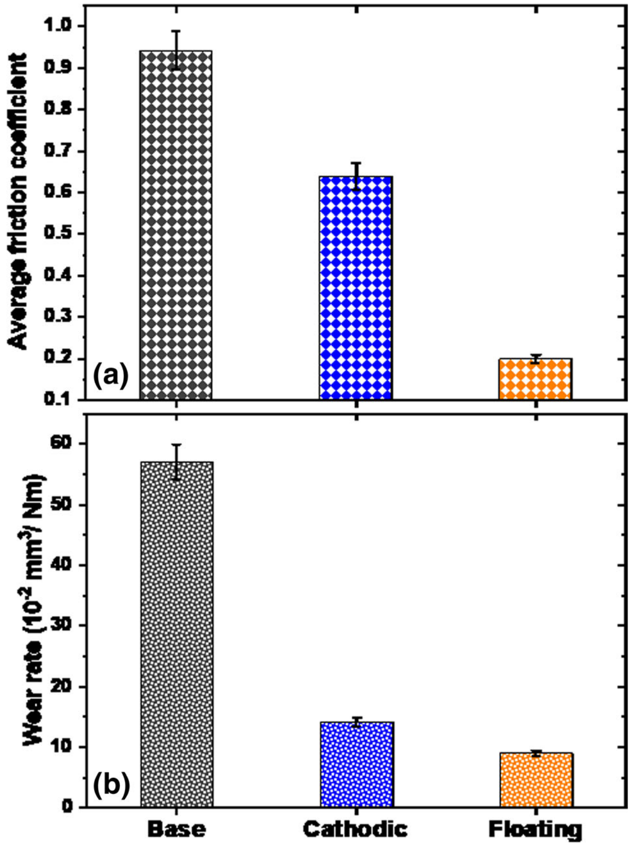

Fig. 11 (a) Average friction coefficient and (b) wear rate of base material, and CCPD samples at cathodic and floating potentials

removed material is presented on the worn tracks as metallic debris. Thus, it indicates that the abrasive wear mechanism is dominant. It happens due to plastic deformation and microplowing of the surface during sliding of the ball. On the other hand, the molybdenum oxide deposited sample wear tracks width is reduced under both conditions. However, the cathodic potential treated sample (Fig. 9b) also displays the grooves due to abrasion and metallic particles on the surface, indicating an abrasive wear mechanism. The high-resolution image shows that surface is damaged due to the sliding of the ball because of plastic deformation. Conversely, the molybdenum oxide deposited under floating potential (Fig. 9c) reveals best wear resistance, and the wear track is narrow and shallow. The track's surface is smooth and clean and does not contain any metallic debris, revealing the adhesive wear is contributing. Thus for tribological purpose, molybdenum oxide film synthesized at floating potential is suitable. It can be attributed to the lubricating performance of molybdenum oxide film (Ref 26). This lubricating film acts as a physical protective film, which avoids direct contact between sliding surfaces during wear analysis and reduces the wear rate (Ref 26). Previously Tang et al. (Ref 26) reported an improvement in anti-wear performance and friction-reducing ability of base oil by adding the molybdenum oxide. The best anti-wear and anti-friction properties were attained by using 0.5 and 0.1 wt.% molybdenum oxide in the base oil. Here, we observed that besides the addition of molybdenum oxide in a base oil to improve the wear properties, the individual deposition of molybdenum oxide coating can improve the wear resistance of AISI-316 steel. The surface images show that the surface of the sample treated at floating potential is smooth and less damaged, representing better wear resistance of this sample. The sample treated at floating potential contains individual molybdenum oxide film (as shown in XRD), and thus it shows better lubricating performance and wear resistance.

The friction coefficient is plotted against the sliding distance for various samples in Fig. 10. The base material's friction coefficient is relatively higher and fluctuating over the treated samples, which shows severe wear. The rapid variation can be attributed to the wear track's oxidation and its removal upon further sliding, as described earlier (Ref 24). The molybdenum oxide deposited sample at cathodic potential depicts that friction coefficient is smooth and low up to a sliding distance of 25 m. Later on, it rises sharply closer to the base material. The initial small and smooth friction coefficient values can be ascribed to the deposited oxide layer having some amount of molybdenum oxide. The rapid rise beyond the 25 m sliding distance can be attributed to the removal of the deposited layer. This fact is well supported by SEM tracks containing the metallic debris and abrasion due to detachment of deposited layer. In contrast, the molybdenum oxide deposited sample at floating potential shows very smooth and very low values of friction coefficient. It is due to the abundant amount of molybdenum oxide on the surface, which work as a solid lubricant and friction-reducing agent during the sliding of the ball on the surface (Ref 26). This result is also well supported by the SEM images of tracks that are clean, smooth, and do not contains metallic particles detached from the worn track. The average values of friction coefficient (Fig. 11a) and wear rate (Fig. 11b) are plotted to compare the wear behavior of deposited films quantitatively. It shows a significant decrease in wear rate and friction coefficient of molybdenum oxide deposited sample, mainly deposited at a floating potential. Thus, it shows that the tribological performance of AISI-316 can improved effectively by molybdenum oxide deposition with CCPN at floating potential.

4. Conclusions

Here, molybdenum oxide is deposited on AISI-316 austenitic stainless steel with the aim to improve the tribological performance for motion-contact parts application. The films are deposited assisted with the low-temperature cathodic cage plasma deposition technique (CCPD) by changing the sample's biasing at floating and cathodic potential. The molybdenum oxide deposited sample under floating potential shows outstanding friction reducing ability and wear resistance. The film deposited on cathodic potential contains a mixture of molybdenum oxide and iron-oxide, while the explicit molybdenum oxide phase is formed on a floating potential treated sample. It suggests that molybdenum oxide deposited at floating potential can be used as a solid lubricant and friction-reducing agent. As this film is successfully deposited on floating potential and it can also be deposited on non-conductors; therefore, it can improve the optical properties of insulators and semiconductors. Advantageously, relatively simple equipment is required in this system, the deposited film is homogenous, the system's efficiency is higher, and low-temperature is required for deposition. This system can be used on industrial-scale applications and is predicted to be efficient.

Acknowledgment

RRMS is thankful to National Council for Scientific and Technological Development (CNPq) for partial financial support. JCDG would like to thank the Mexican National Council for Science and Technology (CONACYT) for the financial support to carry out this research work (Grant No. CB-2015 257705). Dr. Javed Iqbal is thankful to European Regional Development Fund (Project No.1.1.1.5/19/A/003) for the development of quantum optics and photonics at the university of Latvia.

References

1. S.H. Mohamed and S. Venkataraj, Thermal Stability of Amorphous Molybdenum Trioxide Films Prepared at Different Oxygen Partial Pressures by Reactive DC Magnetron Sputtering, *Vacuum*, 2007, **81**(5), p 636–643
2. A.B.V. Leitao, C.L. Lima, B.C. Viana, B. Neto, J.A.P. Costa, T.H.C. Costa, I.A. De Souza, M. Naeem and R.R.M. Sousa, Novel Synthesis of Molybdenum Nitride/oxide on AISI-316 Steel Assisted with Active Screen Plasma Treatment, *Mater. Res. Exp.*, 2019, **6**(11), p 1165
3. Y.J. Lee, Y.I. Seo, S.-H. Kim, D.-G. Kim and Y. Do Kim, Optical Properties of Molybdenum Oxide Thin Films Deposited by á Chemical Vapor Transport of MoO3 (OH) 2, *Appl. Phys. A*, 2009, **97**(1), p 237–241
4. F.F. Ferreira, T.G.S. Cruz, M.C.A. Fantini, M.H. Tabacniks, S.C. de Castro, J. Morais, A. de Siervo, R. Landers and A. Gorenstein, Lithium Insertion and Electrochromism in Polycrystalline Molybdenum Oxide Films, *Solid State Ionics*, 2000, **136**, p 357–363
5. M. Dhanasankar, K. Purushothaman and G.J.A.S.S. Muralidharan, Effect of Temperature of Annealing on Optical, Structural and Electrochromic Properties of Sol–gel Dip Coated Molybdenum oxide Films, *App. Surf. Sci.*, 2011, **257**(6), p 2074–2079
6. S. Kasani, P. Zheng, J. Bright and N. Wu, Tunable Visible-Light Surface Plasmon Resonance of Molybdenum oxide Thin Films Fabricated by E-beam Evaporation, *ACS Appl. Electron. Mater.*, 2019, **1**(11), p 2389–2395
7. F.T. Jaeckel, K.L. Kripps, K.M. Morgan, S. Zhang and D. McCammon, Fabrication of Superconducting Mo/Cu Bilayers using Ion-beam-Assisted e-beam Evaporation, *J. Low Temp. Phys.*, 2016, **184**(3–4), p 647–653
8. C.V. Ramana and C.M. Julien, Chemical and Electrochemical Properties of Molybdenum oxide Thin Films Prepared by Reactive Pulsed-Laser Assisted Deposition, *Chem. Phys. Lett.*, 2006, **428**(1–3), p 114–118
9. A. Hosseinzadeh, M. Nazmabadi and N. Vosoughi, Deposition of Metallic Molybdenum Thin Films on 304L Steel Substrate by SUT-PF, *Surf. Coat. Technol.*, 2017, **309**, p 1052–1061
10. S. Dharmalingam and L. Kong, Chemical Vapor Deposition for Film Deposition, *Encyclopedia of microfluidics and nanofluidics*. D. Li Ed., Springer, New York, 2008, p 255–260
11. L. Xiao, D. Yan, J. He, L. Zhu, Y. Dong, J. Zhang and X. Li, Nanostructured TiN Coating Prepared by Reactive Plasma Spraying in Atmosphere, *Appl. Surf. Sci.*, 2007, **253**(18), p 7535–7539
12. D.-G. Kim, S.H. Kim and Y. Do Kim, Electrochromic Property of MoO3 Thin Films Deposited by Chemical Vapor Transport Synthesis, *Jpn J Appl Phys*, 2011, **50**(10), p 1026
13. H.R. Abedi, M. Salehi, M. Yazdkhasti and A. Hemmasian-E, Effect of High Temperature Post-oxidizing on Tribological and Corrosion Behavior of Plasma Nitrided AISI 316 Austenitic Stainless Steel, *Vacuum*, 2010, **85**(3), p 443–447
14. A. Esfahani, M.H. Sohi, J. Rassizadehghani and F. Mahboubi, Effect of Treating Atmosphere in Plasma Post-oxidation of Nitrocarburized AISI 5115 Steel, *Vacuum*, 2007, **82**(3), p 346–351
15. Z.S. Asadi and F. Mahboubi, Effect of Component's Geometry on the Plasma Nitriding Behavior of AISI 4340 Steel, *Mater. Des.*, 2012, **34**, p 516–521
16. C. Li, T. Bell and H. Dong, A Study of Active Screen Plasma Nitriding, *Surf. Eng.*, 2002, **18**(3), p 174–181
17. T. Fraczek, M. Ogorek, Z. Skuza and R. Prusak, Mechanism of Ion Nitriding of 316L Austenitic Steel by Active Screen Method in a Hydrogen-nitrogen Atmosphere, *Int. J. Adv. Manuf. Technol.*, 2020, **109**(5), p 1357–1368
18. N. Toshioka and A. Nishimoto, Surface-modified Layer formed by Plasma Nitriding using Chromium Screen, *Mater. Trans.*, 2020, **61**, p 1115–1121
19. D. Kovács, J. Dobránszky, T. Fodor, V. Takáts and A. Bonyár, Investigation of the ASPN Process of Low Alloy Steel by using Ni or Cr Coated Active Screens, *Surf. Coat. Technol.*, 2020, **394**, p 125638
20. K. Lin, X. Li, L. Tian and H. Dong, Active Screen Plasma Surface Co-alloying of 316 Austenitic Stainless Steel with both Nitrogen and Niobium for the Application of Bipolar Plates in Proton Exchange Membrane Fuel Cells, *Int. J. Hydrogen Energy*, 2015, **40**(32), p 10281–10292
21. Y. Dong, X. Li, L. Tian, T. Bell, R.L. Sammons and H. Dong, Towards Long-lasting Atibacterial Stainless Steel Surfaces by Combining Double Glow Plasma Silvering with Active Screen Plasma Nitriding, *Acta Biomater.*, 2011, **7**(1), p 447–457
22. Y. Dong, X. Li, T. Bell, R. Sammons and H. Dong, Surface Microstructure and Antibacterial Property of an Active-screen Plasma Alloyed Austenitic Stainless Steel Surface with Cu and N, *Biomed. Mater.*, 2010, **5**(5), p 054105
23. M.S. Libório, G.B. Praxedes, L.L.F. Lima, I.G. Nascimento, R.R.M. Sousa, M. Naeem, T.H. Costa, S.M. Alves and J. Iqbal, Surface Modification of M2 Steel by Combination of Cathodic Cage Plasma Deposition and Magnetron Sputtered MoS2-TiN Multilayer Coatings, *Surf. Coat. Technol.*, 2020, **384**, p 125327
24. M. Naeem, J. Iqbal, M. Zakaullah, M. Shafiq, Z.I. Mujahid, J.C. Díaz-Guillén, C.M. Lopez-Badillo, R.R.M. Sousa and M.A. Khan, Enhanced Wear and Corrosion Resistance of AISI-304 Steel by Duplex Cathodic Cage Plasma Treatment, *Surf. Coat. Technol.*, 2019, **375**, p 34–45
25. M. Naeem, M. Shafiq, M. Zaka-ul-Islam, M.I. Bashir, J.C. Díaz-Guillén, C.M. Lopez-Badillo and M. Zakaullah, Novel Duplex Cathodic Cage Plasma Nitriding of Non-alloyed Steel using Aluminum and Austenite Steel Cathodic Cages, *J. Alloy. Compd.*, 2017, **721**, p 307–311
26. W. Tang, R. Liu, X. Lu, S. Zhang and S. Liu, Tribological Behavior of Lamellar Molybdenum trioxide as a Lubricant Additive, *Materials*, 2018, **11**(12), p 2427
27. D. Sinkeviciute, J. Baltrusaitis and N. Dukstiene, Layered Molybdenum Oxide Thin Films Electrodeposited from Sodium Citrate Electrolyte Solution, *J. Solid State Electrochem.*, 2011, **15**(4), p 711–723
28. W. Liang, Surface Modification of AISI 304 Austenitic Stainless Steel by Plasma Nitriding, *Appl. Surf. Sci.*, 2003, **211**(1–4), p 308–314

29. D.M. Xu, G.Q. Li, X.L. Wan, R.L. Xiong, G. Xu, K.M. Wu, M.C. Somani and R.D.K. Misra, Deformation Behavior of High Yield Strength–high Ductility Ultrafine-Grained 316LN Austenitic Stainless steel, *Mater. Sci. Eng. A*, 2017, **688**, p 407–415
30. P.M.D.O. Silva, H.F.G. de Abreu, V.H.C. de Albuquerque, P. de Lima Neto and J.M.R.S. Tavares, Cold Deformation Effect on the Microstructures and Mechanical Properties of AISI 301LN and 316L Stainless Steels, *Mater. Des.*, 2011, **32**(2), p 605–614
31. Y. Xiong, Y. Yue, Y. Lu, T. He, M. Fan, F. Ren and W. Cao, Cryorolling Impacts on Microstructure and Mechanical Properties of AISI 316 LN Austenitic Stainless Steel, *Mater. Sci. Eng. A*, 2018, **709**, p 270–276
32. M. Hadji and R. Badji, Microstructure and Mechanical Properties of Austenitic Stainless Steels after Cold Rolling, *J. Mater. Eng. Perform.*, 2002, **11**(2), p 145–151
33. Y. Xiong, Y. Yue, T. He, Y. Lu, F. Ren and W. Cao, Effect of Rolling Temperature on Microstructure Evolution and Mechanical Properties of AISI316LN Austenitic Stainless Steel, *Materials*, 2018, **11**(9), p 1557
34. N. Solomon and I. Solomon, Effect of Deformation-induced Phase Transformation on AISI 316 Stainless Steel Corrosion Resistance, *Eng. Fail. Anal.*, 2017, **79**, p 865–875
35. A. Saeed, A. Khan, F. Jan, M. Abrar, M. Khalid and M. Zakaullah, Validity of "Sputtering and Re-condensation" Model in Active Screen Cage Plasma Nitriding Process, *Appl. Surf. Sci.*, 2013, **273**, p 173–178
36. S.C. Gallo and H. Dong, On the Fundamental Mechanisms of Active Screen Plasma Nitriding, *Vacuum*, 2009, **84**(2), p 321–325
37. P. Hubbard, J. Partridge, E. Doyle, D. McCulloch, M. Taylor and S. Dowey, Investigation of Nitrogen Mass Transfer within an Industrial Plasma Nitriding System I: the Role of Surface Deposits, *Surf. Coat. Technol.*, 2010, **204**(8), p 1145–1150
38. M. Berg, C.V. Budtz-Jørgensen, H. Reitz, K.O. Schweitz, J. Chevallier, P. Kringhøj and J. Bøttiger, On Plasma Nitriding of Steels, *Surf. Coat. Technol.*, 2000, **124**(1), p 25–31
39. A. Lassoued, M.S. Lassoued, B. Dkhil, A. Gadri and S. Ammar, Structural, Optical and Morphological Characterization of Cu-doped α-Fe2O3 Nanoparticles Synthesized through Co-precipitation Technique, *J. Mol. Struct.*, 2017, **1148**, p 276–281
40. J.V.B. Moura, J.V. Silveira, J.G. da Silva Filho, A.G. Souza Filho, C. Luz-Lima and P.T.C. Freire, Temperature-induced Phase Transition in h-MoO3: Stability Loss Mechanism Uncovered by Raman Spectroscopy and DFT Calculations, *Vib. Spectrosc.*, 2018, **98**, p 98–104
41. V.V. Atuchin, T.A. Gavrilova, V.G. Kostrovsky, L.D. Pokrovsky and I.B. Troitskaia, Morphology and Structure of Hexagonal MoO 3 Nanorods, *Inorg. Mater.*, 2008, **44**(6), p 622
42. N. Vidakis, A. Antoniadis and N. Bilalis, The VDI 3198 Indentation Test Evaluation of a Reliable Qualitative Control for Layered Compounds, *J. Mater. Process. Technol.*, 2003, **143**, p 481–485
43. S. Taktak and S. Ulu, Wear Behaviour of TRD Carbide Coatings at Elevated Temperatures, *Ind. Lubr. Tribol.*, 2010, **62**(1), p 37–45
44. A.S. Kuprin, A. Gilewicz, T.A. Kuznetsova, V.A. Lapitskaya, G.N. Tolmachova, B. Warcholinski, S.M. Aizikovich and E.V. Sadyrin, Structure and Properties of ZrON Coatings Synthesized by Cathodic Arc Evaporation, *Materials*, 2021, **14**(6), p 1483
45. S. Taktak and S. Tasgetiren, Identification of Delamination Failure of Boride Layer on Common Cr-based Steels, *J. Mater. Eng. Perform.*, 2006, **15**(5), p 570–574
46. G.A. Rodríguez-Castro, L.F. Jiménez-Tinoco, J.V. Méndez-Méndez, I. Arzate-Vázquez, A. Meneses-Amador, H. Martínez-Gutiérrez and I. Campos-Silva, Damage Mechanisms in AISI 304 Borided Steel: Scratch and Daimler-benz Adhesion Tests, *Mater. Res.*, 2015, **18**(6), p 1346–1353
47. C.V. Ramana, V.V. Atuchin, V.G. Kesler, V.A. Kochubey, L.D. Pokrovsky, V. Shutthanandan, U. Becker and R.C. Ewing, Growth and Surface Characterization of Sputter-deposited Molybdenum Oxide Thin Films, *Appl. Surf. Sci.*, 2007, **253**(12), p 5368–5374
48. G. Wang, Y. Ji, L. Zhang, Y. Zhu, P.-I. Gouma and M. Dudley, Synthesis of Molybdenum Oxide Nanoplatelets During Crystallization of the Precursor Gel from its Hybrid Nanocomposites, *Chem. Mater.*, 2007, **19**(5), p 979–981
49. A.K. Prasad, D.J. Kubinski and P.-I. Gouma, Comparison of Sol–gel and Ion Beam Deposited MoO3 Thin Film Gas Sensors for Selective Ammonia Detection, *Sens. Actuators, B Chem.*, 2003, **93**(1–3), p 25–30
50. E. Comini, G. Faglia, G. Sberveglieri, C. Cantalini, M. Passacantando, S. Santucci, Y. Li, W. Wlodarski and W. Qu, Carbon monoxide Response of Molybdenum Oxide Thin Films Deposited by Different Techniques, *Sens. Actuators, B Chem.*, 2000, **68**(1–3), p 168–174
51. A. Fossati, F. Borgioli, E. Galvanetto and T. Bacci, Glow-discharge Nitriding of AISI 316L Austenitic Stainless Steel: Influence of Treatment Time, *Surf. Coat. Technol.*, 2006, **200**(11), p 3511–3517
52. E. Zdravecká, J. Slota, P. Solfronk and M. Kolnerová, Evaluation of the Effect of Different Plasma-nitriding Parameters on the Properties of Low-alloy Steel, *J. Mater. Eng. Perform.*, 2017, **26**(7), p 3588–3596